nature communications

Article

https://doi.org/10.1038/s41467-025-56863-1

Highly enhanced room-temperature single-atom catalysis of two-dimensional organic-inorganic multiferroics Cr(half-fluoropyrazine)$_2$ for CO oxidation

Received: 19 August 2024

Accepted: 3 February 2025

Published online: 12 February 2025

Check for updates

Feixiang Zhang[1,4], Panshuo Wang[1,4], Yandi Zhu[1], Jinlei Shi[1,2], Rui Pang[1], Xiaoyan Ren[1] ✉ & Shunfang Li[1,3] ✉

In modern chemistry, the development of highly efficient room-temperature catalysts is of great significance and remains a long-standing challenge in various typical reactions. Here, we theoretically demonstrate that the two-dimensional (2D) multiferroic, Cr(half-fluoropyrazine)$_2$ [Cr(h-fpyz)$_2$], is a promising single-atom catalyst (SAC) operating at room temperature for CO oxidation. The rate-limiting barrier is merely 0.325 eV, leading to a reaction rate (i.e., 3.47×10^6 s^{-1}) of six orders of magnitude higher than its monoferroic derivative [Cr(pyz)$_2$], due to the synergetic effects of two aspects. First, the more flexible ligand rotations in Cr(h-fpyz)$_2$ facilitate the activation of O_2 molecule, simultaneously enhancing the charge transfer and spin-accommodation process. Second, on Cr(h-fpyz)$_2$, O_2 adsorption induces a distinctly lower local positive electric field, reducing the electrostatic repulsion of the polar CO molecule. These findings may also pave the way for establishing highly efficient SAC platforms based on 2D multiferroics where multidegree of freedom (e.g., spin, polarity) synergistically matter.

With the rapid advancement of modern industry and the intensifying energy crises, the development of highly efficient catalysts has become critically important for a range of complex chemical reactions. However, most catalysts encounter complex stability issues, and their practical applications are also generally constrained by the relatively high operating temperature[1,2]. The U.S. Department of Energy (US-DOE) has set the goal of achieving 90% conversion of all criteria pollutants at 150 °C—"the 150°C challenge"[3]. Nevertheless, such a temperature is still ~100 °C lower than current state-of-the-art commercial automotive catalysts. In general, charge[4], spin[5], orbital[6], and polarity[7] can simultaneously play significant roles in chemical processes. Correspondingly, if a catalytic platform possesses well-matched degrees of freedom, such as spin and polarity, with those of the reactants, high-performance selective catalysis can be achieved[8–10]. Recent reports have demonstrated that high spin states of the catalysts can significantly enhance various chemical processes[8–10], which can be effectively explained by Wigner's spin selection rule[9,11–15]. Moreover, recent advances have confirmed that electric field[16,17] and ferroelectricity can play a crucial role in enhancing catalytic activities, such as CO_2 electrocatalytic reduction[18] and photocatalytic water splitting[19]. This enhancement is primarily due to the significantly improved charge transfer facilitated by ferroelectric materials[20]. Therefore, developing highly efficient room-temperature catalysts leveraging the synergetic effects of the aforementioned degrees of freedom is both anticipated and warranted.

[1]Key Laboratory of Material Physics, Ministry of Education, School of Physics, Zhengzhou University, Zhengzhou, China. [2]College of Physics and Electronic Engineering, Zhengzhou Normal University, Zhengzhou, China. [3]Institute of Quantum Materials and Physics, Henan Academy of Sciences, Zhengzhou, China. [4]These authors contributed equally: Feixiang Zhang, Panshuo Wang. ✉e-mail: renxyan@zzu.edu.cn; sflizzu@zzu.edu.cn

Multiferroics, which simultaneously encompass ferroelectric, ferromagnetic, and ferroelastic orders, have attracted significant attention from researchers due to their promising applications in various fields[21–23]. These applications include nonvolatile multistate data storage, magnetoelectric sensors, and multifunctional and electrically controlled spin wave devices[24,25]. Moreover, due to the tunable orders and the synergies of different degrees of freedom, such as charge, spin, and orbital integrated within a single phase, it is reasonable to expect that multiferroics could serve as highly efficient room-temperature catalytic candidates. Very recently, a new type of two-dimensional (2D) multiferroic material, *i.e.*, a 2D metal-organic framework (MOF) room-temperature multiferroicity (RT-MF), specifically $Cr(h\text{-}fpyz)_2$ (h-fpyz = half-fluoropyrazine)[26] has been predicted, with stable ferroelectric and ferrimagnetic phase up to around 400 and 600 K, respectively. This unique 2D material can be rationally designed by introducing relatively large ferroelectricity (4.8 μC/cm^2) through fluorination[27–29] in $Cr(pyz)_2$, while retaining the ferromagnetic coupling (3.61 μ_B/Cr) between the evenly dispersed metal ions. Essentially, this 2D RT-MF structure can be understood as a derivative of the experimentally fabricated bulk metal-organic ferrimagnetic layered material ($Li_{0.7}[Cr(pyz)_2]Cl_{0.7}$•0.25(THF))[30], exhibiting a high Curie critical temperature of up to 515 K and significant coercivity (7500 Oersted) at room temperature. In recent decades, MOF structures have been widely applied in various fields, such as ferroelectricity[31], sensors[32], and photocatalysis[33]. Moreover, from a geometric perspective, the present 2D RT-MF $Cr(h\text{-}fpyz)_2$ MOF structure, featuring evenly dispersed Cr species in single-atomic form stabilized by surrounding organic ligands, represents a promising candidate for high-loading single-atomic catalyst (SAC). SAC represents an important enabling concept[34] and has been intensively exploited in the broad field of chemical catalysis, such as CO_2 reduction[35], CO oxidation[36,37], O_2 reduction[38], N_2 reduction[39], hydrogen evolution reaction[40], and oxygen evolution reaction[41]. Furthermore, by probing the interactions between the single-atom reactive sites and the reactants, multiple potential physical mechanisms have been established from various perspectives. For example, insights from the aspects of geometric flexibility[42,43], charge transfer[44,45], orbital hybridizations[46,47], and spin selection[48,49] have been proposed. However, in these related investigations, the materials used as SAC platforms typically exhibit only one type of ferroic order, such as ferromagnetism[50,51], or ferroelectricity[52,53]. To date, despite extensive research on the distinctive physical properties of both 2D multiferroic materials[54–56], and the catalysis of numerous SAC systems[6,34], the synergetic effect of these aspects on the room-temperature catalytic performance of 2D RT-MF SAC structures, such as $Cr(h\text{-}fpyz)_2$, remains significantly underexplored.

Here, employing state-of-the-art first-principles calculations and model analysis, taking spin-triplet O_2 activation and polar molecule CO oxidation as a prototypical example, we demonstrate that the present 2D RT-MF $Cr(h\text{-}fpyz)_2$ can serve as a highly efficient SAC candidate operating at room temperature. The calculated rate-limiting energy barrier is 0.325 eV, resulting in a reaction rate of $3.47 \times 10^6\ s^{-1}$ at 300 K. This rate is six orders of magnitude higher than its monoferroic derivative $[Cr(pyz)_2]$ counterpart, due to the synergetic effects of magnetism and ferroelectricity. Specifically, the flexible rotation of the organic ligand in the multiferroic $Cr(h\text{-}fpyz)_2$ functions as a controllable knob, enhancing the charge transfer and spin accommodation during the activation of spin-triplet O_2 molecule, while simultaneously lowering the local normal positive electric field. This synergetic mechanism results in the polar CO molecule experiencing relatively low repulsive electrostatic interactions and a significantly reduced reaction barrier, making the 2D RT-MF $Cr(h\text{-}fpyz)_2$ a promising candidate for a room-temperature SAC system. Beyond their various applications due to their exotic physical properties, the present findings significantly broaden the potential applications of 2D multiferroics in the crucial field of chemical catalysis. Moreover, this work may direct new avenues toward developing highly efficient SAC platforms for various other important chemical processes where multiple degrees of freedom, such as spin and polarity, synergistically matter.

Results

Geometric and electronic structures of the 2D RT-MF $Cr(h\text{-}fpyz)_2$

First, we briefly reexamined the optimized geometric structure of the 2D $Cr(h\text{-}fpyz)_2$[26] metal-organic framework, simulated within a unit cell comprising four Cr metal atoms and eight h-fpyz organic ligands. Here, four of the latter are connected to the central Cr atoms in a clockwise manner, as indicated by the curved arrows in Fig. 1a. Furthermore, it has been identified that the 2D $Cr(h\text{-}fpyz)_2$ system exhibits an antiferroelectric (AFE) state, due to the antiparallel arrangements of the eight h-fpyz ligand molecules in the primitive cell, as illustrated by the thick arrows in Fig. 1a. Our extensive spin-polarized density-functional theory (DFT) calculations confirmed that in the 2D $Cr(h\text{-}fpyz)_2$ structure, Cr ions exhibit a preference for ferromagnetic order over antiferromagnetic order by about 0.25 eV/f.u., consistent with prior research findings[26]. Moreover, the calculated magnetic moment (MM) of each four-coordinated Cr ion is about 3.68 μ_B, which is antiparallel to that of its four adjacent h-fpyz ligand molecules (Fig. 1b), each possessing an MM of 0.84 μ_B. Thus, the ground state of 2D $Cr(h\text{-}fpyz)_2$ is ferrimagnetic, with a total MM of approximately 8.0 μ_B per primitive unit cell. Figure 1c shows the side view of $Cr(h\text{-}fpyz)_2$. The spin-polarized band structure and density of states (DOS) (Fig. 1d) demonstrate a direct energy band gap of approximately 0.55 eV, which aligns with previous DFT calculations[26].

Activation of spin-triplet O_2 on 2D $Cr(h\text{-}fpyz)_2$

Subsequently, we investigate the adsorption and activation of spin-triplet O_2 on 2D $Cr(h\text{-}fpyz)_2$, which is the key step for CO oxidation. It is revealed that the O_2 molecule preferentially adsorbs on the Cr_I site, with an adsorption energy (E_{ads}) of 1.096 eV. This adsorption is accompanied by a significant increase in the O-O bond length from 1.24 to 1.44 Å (Fig. 1e). Here, we define $E_{ads} = -[E(O_2\text{-}Cr(h\text{-}fpyz)_2) - E(O_2) - E(Cr(h\text{-}fpyz)_2)]$. On Cr_{II} and Cr_{III}, the calculated E_{ads} are relatively low, 0.676 and 0.353 eV, respectively. These distinct adsorption behaviors at the three different sites can be attributed to the contrasting local geometric environments of the antiferroelectric state in the 2D RT-MF $Cr(h\text{-}fpyz)_2$ structure. Specifically, on Cr_I, Cr_{II}, and Cr_{III}, the adsorbed O_2 is surrounded by four H atoms, two H and two F atoms, and four F atoms of the four organic ligands, respectively (Supplementary Fig. 1). In other words, the incoming O_2 molecule may experience disparate local electric field (LEF) nearby (~ 3 Å) above the Cr_I and Cr_{III} atoms, as demonstrated in Fig. 2a, d and Supplementary Fig. 2. This directly influences the charge transfer as detailed shortly, as also supported by the density of states analysis performed in Supplementary Fig. 3, which accounts for the distinct activities of these two types of Cr single-atom reactive sites. These findings strongly indicate that the catalysis of ferroelectric materials[25–28] can be effectively modulated by the ferroelectric polarization direction down to the single-atom scale, specifically in SAC systems. Note that, here the spin-orbit coupling (SOC) effect has a negligible influence on O_2 adsorption and activation. Therefore, the subsequent calculations were performed without considering SOC.

Second, we conduct Bader charge analysis to examine the charge transfer ($\Delta\rho = \rho(O_2\text{-}Cr(h\text{-}fpyz)_2) - \rho(O_2) - \rho(Cr(h\text{-}fpyz)_2)$) between the incoming O_2 and the $Cr(h\text{-}fpyz)_2$ catalytic substrate. Here, $\rho(O_2)$ and $\rho(Cr(h\text{-}fpyz)_2)$ represent the calculated charge obtained from the isolated ground-state O_2 molecule and the 2D $Cr(h\text{-}fpyz)_2$ substrate, respectively. To gain a clearer understanding of the charge transfer, we conducted a Bader charge analysis on the 2D $Cr(h\text{-}fpyz)_2$ substrate (Supplementary Fig. 4). Briefly, in this pristine 2D RT-MF, both nitrogen (N) and fluorine (F) atoms

accommodate charge transferred predominantly from their neighboring chromium (Cr) atoms, amounting to approximately 1.3 |e|, as well as from carbon (C) atoms. Here, C atoms can be classified into two types, which are coordinated by H and F atoms, termed C_H and C_F, respectively. The nearest neighboring C_H and C_F of Cr_I (Cr_{II}) donate about 0.46 (0.36) and 1.09 (0.99) |e|, respectively. Note that, when the incoming O_2 molecule is positioned more than 10 Å above the designated Cr_I active site, as termed the initial state (IS), negligible charge transfer is observed between O_2 and the substrate (Supplementary Fig. 5a). Upon O_2 adsorption on the reactive Cr_I (Cr_{III}) hosting site, approximately 1.02 (0.79) |e| is transferred from the substrate to O_2 respectively (Fig. 2b, e). Such a distinct charge transfer between Cr_I and Cr_{III} accounts for their contrasting catalytic behaviors in CO oxidation, as discussed later. In this process, the reactive Cr_I (Cr_{III}) atom, along with the remaining C, H, and F (C, N, and F) atoms donate electrons by approximately 0.23, 0.69, 0.31, and 0.06 |e| (0.21, 0.39, 0.16, and 0.08 |e|), respectively. Furthermore, Cr_{II} and Cr_{III} (Cr_I and Cr_{II}), which are positioned approximately 7.02 and 9.92 Å (9.92 and 7.02 Å) away from Cr_I (Cr_{III}), respectively contribute negligible charge transfer to the adsorbed O_2. It is noteworthy that, although the Cr_I reactive site is directly linked by the N atom of the h-fpyz ligand, the second nearest neighboring C atoms of Cr_I, in other words, the nearest neighboring C atoms of Cr_{II}, dominate the charge transfer to the adsorbed O_2 (Supplementary Fig. 6). In addition due to the significantly lower electronegativity of H than that of F, the nearby H atoms donate significantly more charge to the adsorbed O_2 species than F atoms. This further rationalizes the contrasting E_{ads} of the O_2 on Cr_I, Cr_{II}, and Cr_{III} sites.

In contrast to charge transfer, the reactive Cr_I atom, along with the substrate N, and C atoms, play a crucial synergetic role in accommodating the spin transferred from the adsorbed O_2 molecule. This facilitates its spin triplet-to-singlet activation of the O_2 molecule, which is the key step for CO oxidation. Similar to the definition of charge transfer $\Delta\rho$, here we define the magnetic moment transfer as $\Delta M = M(O_2 - Cr(h\text{-}fpyz)_2) - M(O_2) - M(Cr(h\text{-}fpyz)_2)$. The initial state (IS) primarily reflects the intrinsic magnetic moment of the incoming spin-triplet O_2 molecule and the substrate (Supplementary Fig. 5b), with negligible interactions between them. Upon O_2 adsorption, the total magnetic moment of the optimized O_2-Cr(h-fpyz)$_2$ complex remains at 8 μ_B (spin quantum number $S_{O_2-Cr(h-fpyz)_2} = 4$). That is, the spin–spin coupling between the spin-triplet O_2 molecule ($S_{O_2} = 1$) and the Cr(h-fpyz)$_2$ catalyst ($S_{Cr(h-fpyz)_2} = 4$) follows the channel of "1 + 4 = 4", which is a spin-allowed reaction according to Wigner's spin selection rule[9,11–15]. Such a classic rule restricts that the total spin quantum number $S_{O_2-Cr(h-fpyz)_2}$ in the spin-allowed reaction should satisfy $S_{O_2-Cr(h-fpyz)_2} = |S_{Cr(h-fpyz)_2} - S_{O_2}|, |S_{Cr(h-fpyz)_2} - S_{O_2}| + 1, \ldots, |S_{Cr(h-fpyz)_2} + S_{O_2}|$, where $S_{Cr(h-fpyz)_2}$ and S_{O_2} are the spin quantum numbers of the substrate Cr(h-fpyz)$_2$ and an isolated ground state O_2 molecule, respectively.

However, the local spin moment of the optimized O_2-Cr(h-fpyz)$_2$ complex with O_2 adsorbed on Cr_I (Cr_{III}) reactive site changes intriguingly, as shown in Fig. 2c (f). Specifically, the magnetic moment of the adsorbed O_2 on Cr_I (Cr_{III}) is reduced from 2.0 μ_B to nearly zero, i.e.,

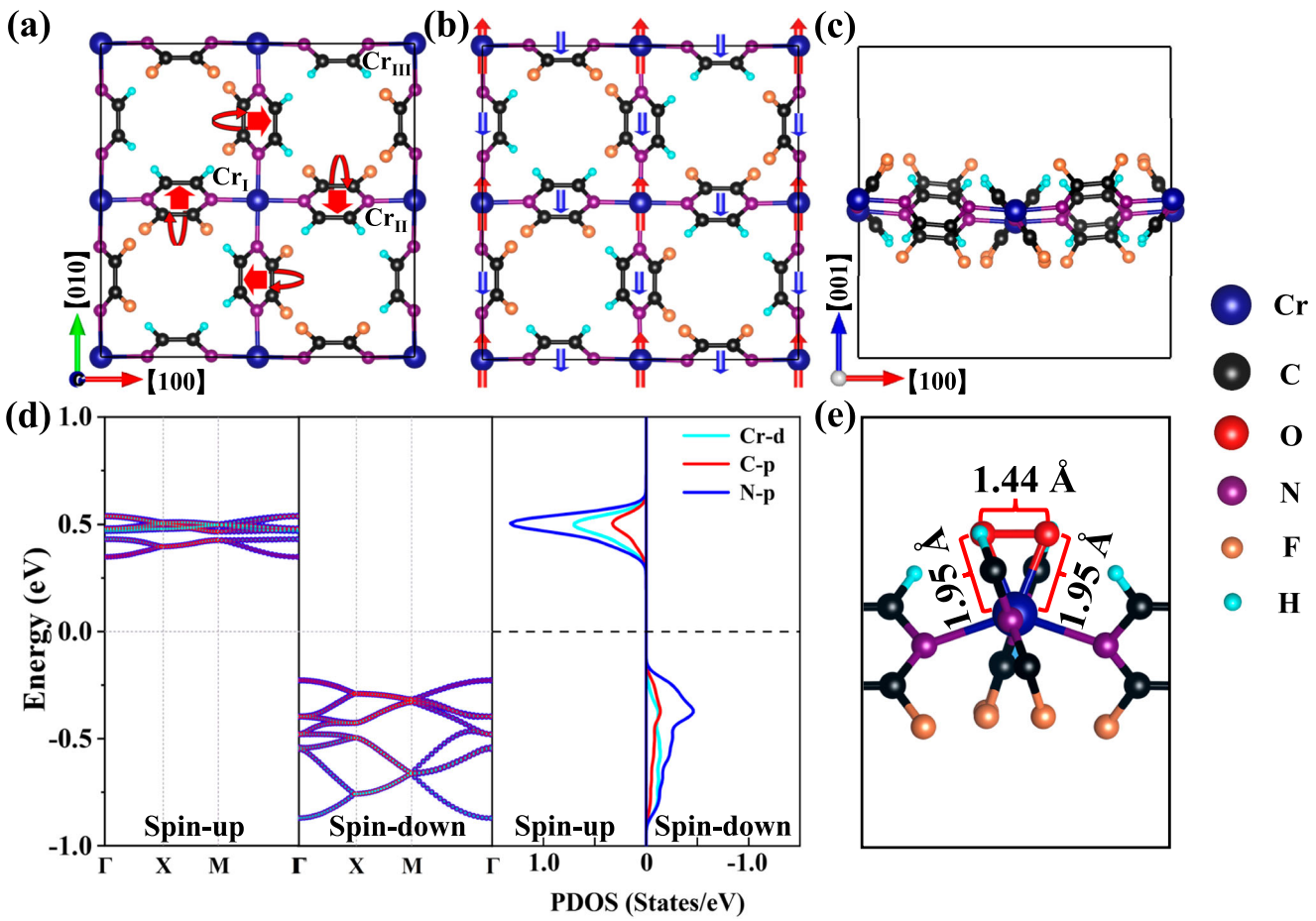

Fig. 1 | Geometric and electronic structures of Cr(h-fpyz)$_2$. In (**a**), the curved red arrow indicates the tilted orientation of the h-fpyz ligands. Here, the center and edge Cr atoms of the primitive cell are termed Cr_I and Cr_{II}, respectively, and the rest of the Cr atoms are termed Cr_{III}. The dipoles of h-fpyz molecules are also schematically indicated by the red thick arrow. In (**b**), the quantity and direction of the magnetic moments are illustrated. **c** Side view of Cr(h-fpyz)$_2$. **d** Energy band structures and projected density of state (PDOS) of Cr(h-fpyz)$_2$. **e** Side view of the optimal local structure of O_2 adsorption on Cr(h-fpyz)$_2$.

https://doi.org/10.1038/s41467-025-56863-1

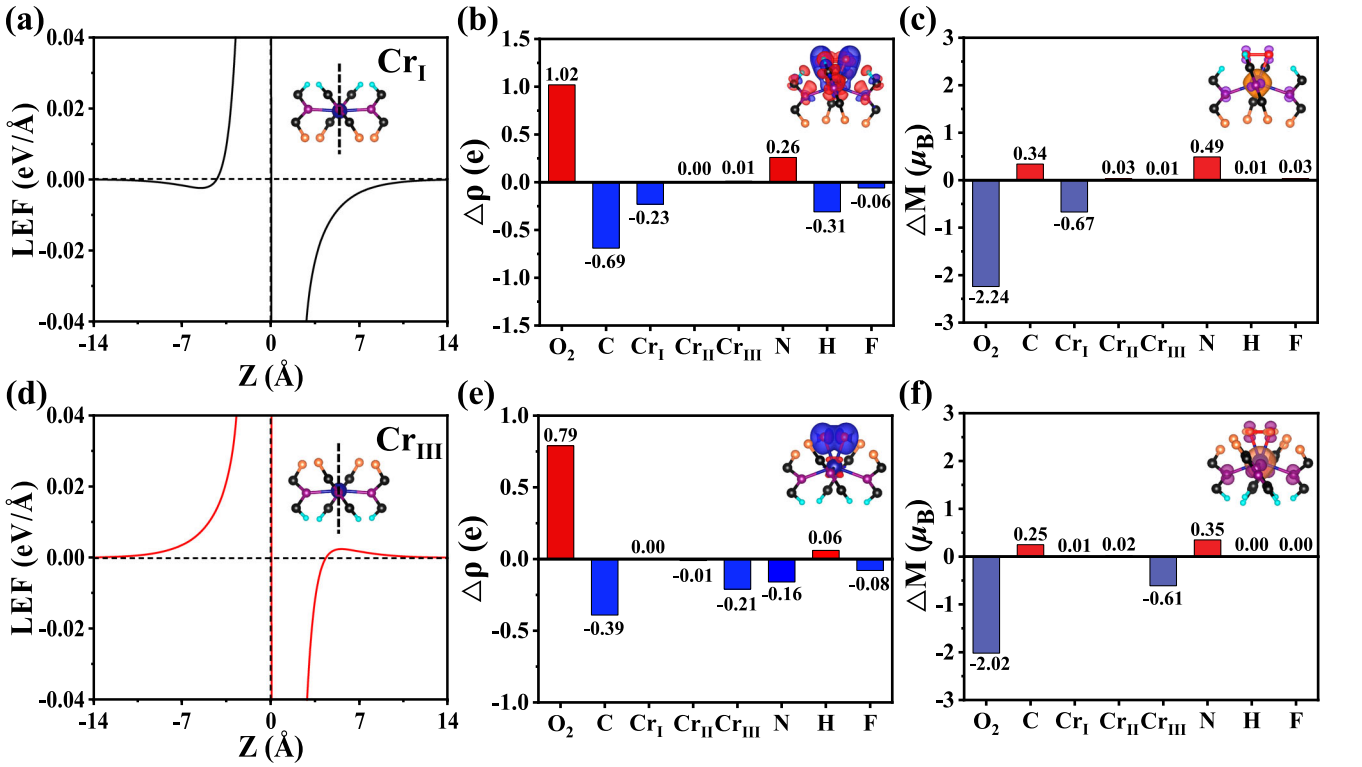

Fig. 2 | Local electric field (LEF), charge transfer (Δρ) and magnetic moment changes (ΔM) upon O_2 adsorption. LEF distributions along the *Z* direction passing through the two representative types of Cr reactive atom (Cr_I and Cr_{III}) in pristine 2D RT-MF Cr(h-fpyz)$_2$, Δρ and ΔM are calculated on the optimized structure when an O_2 molecule is adsorbed on the Cr reactive site performed by Bader analysis. The iso-surface value is 0.0198 e/Å^3. **a**–**c** for the case of Cr_I, and (**d**–**f**) for the case of Cr_{III}. In (**a**) and (**d**), Cr atoms are set as the position references.

−0.24 (−0.02) μ_B, indicating that the O_2 molecule has transitioned from a spin triplet state to singlet. Correspondingly, the magnetic moment of the Cr_I (Cr_{III}) atom is reduced from 3.68 (3.69) to 3.01 (3.08) μ_B, with a reduction of 0.67 (0.61) μ_B. Somewhat unexpectedly, the nearby non-metal atoms, such as C and N, in the vicinity of the reactive Cr_I (Cr_{III}) atom primarily accommodate the magnetic moments by 0.83 (0.60) μ_B. However, the relatively distant transitional metal atoms, Cr_{II} and Cr_{III} (Cr_I and Cr_{II}) only accommodate about 0.04 (0.03) μ_B upon O_2 adsorption and activation. These results demonstrate a significant synergetic spin communication mechanism among the O_2 molecules, the substrate *p*-block C/N atoms, and the *d*-block Cr reactive site in the activation of spin-triplet O_2. Collectively, comparing the cases of O_2 adsorption on Cr_I and Cr_{III}, it is evident that the reactivity of the Cr atom increases with the synergy of charge transfer and spin communication involving the *p*-block C/N atoms. Moreover, there is a significant linear scaling relationship[9,57] between the E_{ads} of the O_2 molecule and the magnetic changes of different Cr reactive sites and the nonmetal atoms as well, as detailed in Supplementary Fig. 7. According to Wigner's spin selection rule, the catalytic system in a low spin state ($S = 0$) typically exhibits high inertness toward spin-triplet O_2[13,14]. This observation convincingly demonstrates the crucial role of the magnetic order of the 2D RT-MF Cr(h-fpyz)$_2$ in facilitating the activation of the ground state O_2 molecule.

CO oxidation on 2D Cr(h-fpyz)$_2$

Now, we continue to examine the minimum energy pathway (MEP) of CO oxidation on 2D Cr(h-fpyz)$_2$ (step i, Fig. 3) via interacting with the adsorbed O_2 molecule (step ii, Fig. 3). Note that, here we have also verified the CO adsorption on the pristine Cr(h-fpyz)$_2$, and the optimized E_{ads}(CO) is merely about 0.367 eV, which is much lower than that of $E_{ads}(O_2) = 1.096$ eV. Therefore, for the present system, CO oxidation should prefer the E-R reaction mechanism with O_2 preferentially adsorbed. It is observed that the adsorbed O_2 molecule is readily attacked by the incoming CO, releasing a CO_2 molecule upon overcoming a low activation energy (E_{bar}) of 0.325 eV (TS_1, Fig. 3), with an exothermic energy of 2.799 eV. In TS_1, the distance between CO and O is 2.0 Å. Following the release of the generated CO_2 molecule, an O species is left on the Cr_I site (step iv, Fig. 3). Consequently, the second incoming CO can also smoothly react with the protruding O atom, generating another CO_2 precursor with an exothermic energy of 2.454 eV after overcoming an even lower E_{bar} of 0.298 eV (TS_2, Fig. 3). Further calculations demonstrate that the desorption energy of the second CO_2 (step vi, Fig. 3) is fairly low, ~0.2 eV. Correspondingly, the low rate-limiting energy barrier of 0.325 eV results in a high reaction rate of about $3.47 \times 10^6\ s^{-1}$ at room temperature (300 K), as estimated by using the Arrhenius form[58] ($R = R_0 \times \exp[-E_{bar}/(k_BT)]$) with a typical prefactor R_0 of $10^{12}\ s^{-1}$. Such a low rate-limiting E_{bar} of 0.325 eV is significantly lower than those obtained for various other typical high-efficient noble SACs or nanocluster-based catalytic complexes, e.g., 0.79 eV for Pt_1/FeO_x[34], 0.91 eV for Pt_1/Fe_2O_3[59], 0.56 eV for Pt_1/CeO_2[60], 1.1 eV for Ir_1-on-$MgAl_2O_4$[61], 0.66 eV for Pt_4/CoNi@C[62], and 1.71 eV for Pt-carbonyl[63], respectively. Moreover, the calculated R ($E_{bar} = 0.325$ eV) reaches $1.34 \times 10^8\ s^{-1}$ at 423 K, implying that the present 2D RT-MF Cr(h-fpyz)$_2$ is a promising high-performance catalyst subject to "the 150 °C challenge".

As a comparison, we have also examined CO oxidation via interacting with the adsorbed O_2 on Cr_{II} and Cr_{III} single-atom reactive sites, as detailed in Supplementary Fig. 8. Briefly, on Cr_{II} and Cr_{III}, the relatively high rate-limiting E_{bar} of 0.582 and 1.098 eV result in low reaction rates of about 1.67×10^2 and $3.57 \times 10^{-7}\ s^{-1}$ at room temperature, respectively. Especially compared to Cr_I, reversing the LEF direction around the Cr_{III} single-atom reactive site significantly (see Fig. 2a and d) reduces the reaction rate, by approximately thirteen orders of amplitude. Note also that, in consideration of the zero-point energy and entropy contributions, on the two representative

https://doi.org/10.1038/s41467-025-56863-1

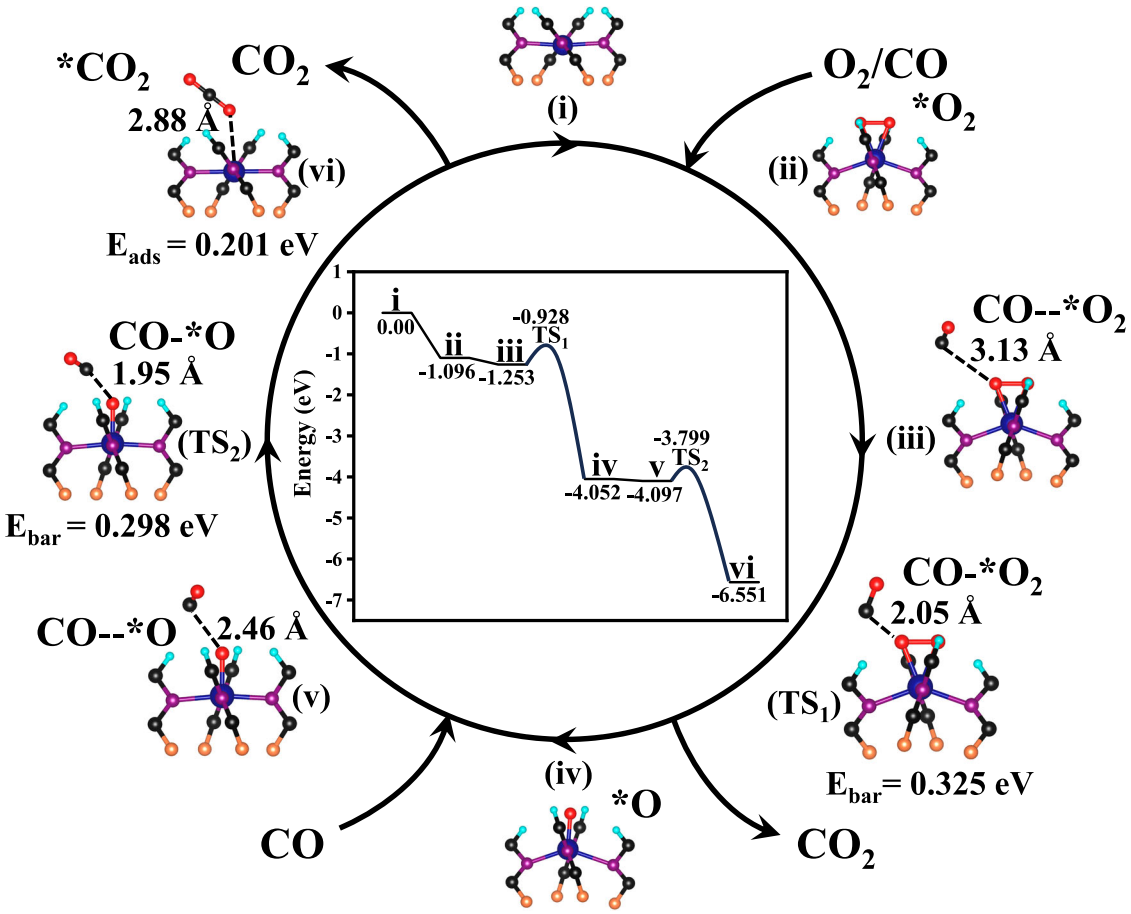

Fig. 3 | Catalytic pathway for CO oxidation. Minimum energy pathway (MEP) for O_2 activation and CO oxidation via the Eley-Rideal (E-R) mechanism on Cr_I reactive site in $Cr(h\text{-}fpyz)_2$, with the energy activation barrier (E_{bar}) indicated. Here, $*O_2(O)$ denotes the adsorption of $O_2(O)$ on the catalytic substrate. $CO\text{--}*O_2(O)$ and $CO\text{-}*O_2(O)$ correspond to the relatively weak and strong interactions between the CO and the adsorbed $O_2(O)$ species.

reactive sites of Cr_I and Cr_{III}, the E_{bar} is increased by 38 and 115 meV, respectively. Correspondingly, the calculated reaction rates of these two cases become 7.97×10^5 and 4.18×10^{-9} s^{-1} at 300 K, respectively. These findings convincingly confirm that an on-off switching for the room-temperature catalysis of SAC can be achieved by tuning the polar direction of the 2D RT-MF $Cr(h\text{-}fpyz)_2$. The Cr_{II} reactive site positions intermediately between Cr_I and Cr_{III} due to its intermediate LEF feature as compared to the latter two cases, see also Supplementary Fig. 2.

Figure 4a presents the Bader charge analysis for the key steps in CO oxidation depicted in Fig. 3. When CO is weakly adsorbed in the vicinity of the adsorbed O_2 (step iii, Fig. 3), the O_2-CO species acquires a charge of approximately 1.04 |e|. Specifically, the non-metal atoms in the substrate contribute about 0.81 |e|, whereas the metal Cr atoms contribute only about 0.23 |e|, indicating that the non-metal atoms dominate the charge transfer. This trend is also observed in TS_1 and all other representative steps up to TS_2 (Fig. 3), as also demonstrated in Fig. 4a and Supplementary Fig. 9a.

The changes in the magnetic moment (ΔM) of the corresponding key steps are analyzed in Fig. 4b. From step iii to step vi, there are substantial reductions in the local magnetic moments of both the O_2-CO species and the Cr metal atoms. Notably, as in step iii, in almost all the other key steps, the *p*-block non-metal C and N atoms accommodate more MM than that of the *d*-block Cr reactive atom (Supplementary Fig. 9b). These findings demonstrate a delicate synergetic charge and spin accommodation mechanism occurred among the O_2/CO molecule, *d*-block reactive Cr atom, and the surrounding *p*-block C and N atoms, occurring during both O_2 activation and CO oxidation on the multiferroic $Cr(h\text{-}fpyz)_2$ catalytic platform.

Comparison of CO oxidation on monoferroic $Cr(pyz)_2$

To more clearly demonstrate the crucial role of the multiferroic orders in high-performance CO oxidation, we conducted a comparative examination of O_2 activation and CO oxidation on $Cr(pyz)_2$ (pyz = pyrazine). This compound was created by substituting all the F atoms in $Cr(h\text{-}fpyz)_2$ with H atoms (Supplementary Fig. 10a, b). Consequently, the substrate undergoes a transition from multiferroic to monoferroic, remaining only ferrimagnetic properties. Based on this, we further explored the adsorption of O_2 on the monoferroic $Cr(pyz)_2$ substrate (Supplementary Fig. 10c). In comparison to the adsorption on the Cr_I reactive site of multiferroic $Cr(h\text{-}fpyz)_2$, the optimized $E_{ads}(O_2)$ increases slightly by 0.040 eV to reach 1.136 eV. In addition, the O-O bond length is enlarged to 1.44 Å. Similarly, CO exhibits weak adsorption on the Cr atom, characterized by an $E_{ads}(CO)$ of 0.383 eV, suggesting that only an E-R mechanism is viable for CO oxidation. Surprisingly, despite comparable activation of O_2 on both catalytic platforms in terms of bond length and adsorption energy, a significantly elevated rate-limiting E_{bar} of 0.659 eV is observed for CO oxidation on the monoferroic $Cr(pyz)_2$ (Supplementary Fig. 11). Using the same approach, the calculated CO oxidation rate is 8.48×10^0 s^{-1}, which is about six orders of magnitude lower than that observed on the 2D RT-MF $Cr(h\text{-}fpyz)_2$ at the room temperature. These findings further underscore the pivotal role of multiferroicity in enhancing the catalytic performance of the present 2D material for CO oxidation.

https://doi.org/10.1038/s41467-025-56863-1

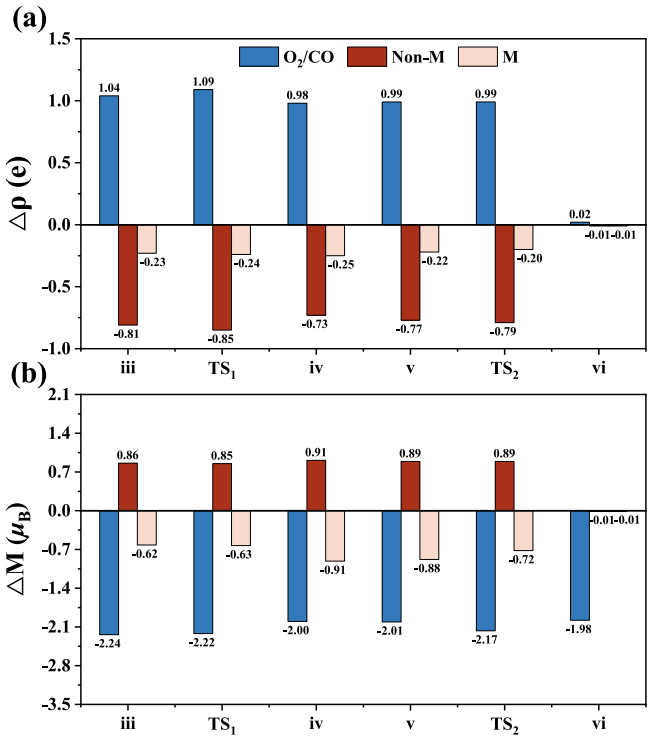

Fig. 4 | Changes in charge and magnetic moment during key steps of the CO oxidation. a Charge transfer (Δρ) and (**b**) magnetic moment changes (ΔM) of the key steps, including the transition states (TS) during catalytic CO oxidation. In this context, red, orange, and peach represent non-metal (Non-M) and metal (M) elements respectively. And the O_2-CO species is identified in sky blue.

Role of ligand rotation in LEF: A knob for on-off switching room-temperature catalysis

To further elucidate the observed phenomena, we conducted a comparative analysis of the local geometric structures around the Cr reactive site in multiferroic Cr(h-fpyz)$_2$ and monoferroic Cr(pyz)$_2$, both with and without O_2 adsorption (Fig. 5). Initially, in the case of 2D RT-MF Cr(h-fpyz)$_2$, prior to O_2 adsorption, each of the four h-fpyz ligands surrounding the Cr reactive site tilts approximately 37.8° away from the (100) plane (Fig. 5a) or the (010) plane (Fig. 5b). However, upon O_2 adsorption, the angles undergo symmetry-breaking evolution into two distinct classes. Specifically, the angles between the two h-fpyz rings connecting the reactive Cr atoms along [010] ([100]) direction and the (100) ((010)) plane are significantly reduced (slightly enlarged) from 37.8° to 19.3° (37.8° to 38.5°), (Fig. 5a, b). This change in orientation can be attributed in part to the electrostatic attractive interactions between the negatively charged O_2 and the nearby H cations, and the smooth tunability and adaptability of the organic ligands as well, as detailed in Supplementary Fig. 12.

Meanwhile, as illustrated in the corresponding lower panels, the position of the reactive Cr atom undergoes spontaneous changes along the [001] direction relative to the pristine Cr(h-fpyz)$_2$ substrate. Specifically, the Cr atom shifts upward, displaying significant displacements relative to the mass centers of the N atom along the [010] and [100] directions (Fig. 5a, b). For instance, following O_2 adsorption (structure ii), the Cr atoms shifted modestly (considerably) upward by approximately 0.24 (0.81) Å. Similar contrasting phenomena are also observed during other critical stages of the CO oxidation process, including TS_1, iv, TS_2, and vi (Supplementary Fig. 13). Furthermore, qualitatively similar findings are confirmed for O_2 adsorption and CO oxidation on the monoferroic Cr(pyz)$_2$. Specifically, the angles (about 47.5°) with respect to (100) ((010)) plane are slightly reduced (enlarged) to 33.6° (47.8°) (Fig. 5c, d). Meanwhile, the Cr reactive site

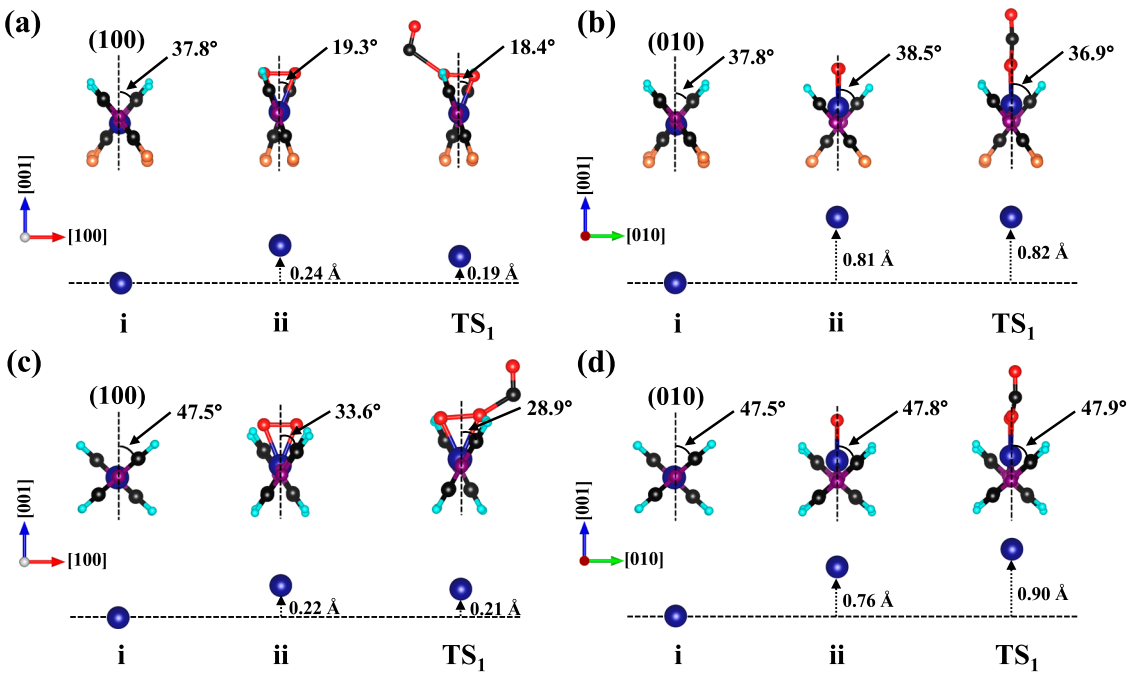

Fig. 5 | Local structural changes around the active sites of Cr(h-fpyz)$_2$ and Cr(pyz)$_2$. a, **b** Local geometric structures around the Cr reactive site of the multiferroic Cr(h-fpyz)$_2$ and (**c**, **d**) Monoferroic Cr(pyz)$_2$ with (step i) and without (step ii, the first transition state (TS_1)) O_2 adsorption viewed from the (**a**, **c**) [010] and (**b**, **d**) [100] directions, respectively. The lower panels illustrate the displacements of the Cr atoms along the [001] direction relative to the distinct mass centers of the N atoms along the (**a**, **c**) [010] and (**b**, **d**) [100] directions, respectively.

https://doi.org/10.1038/s41467-025-56863-1

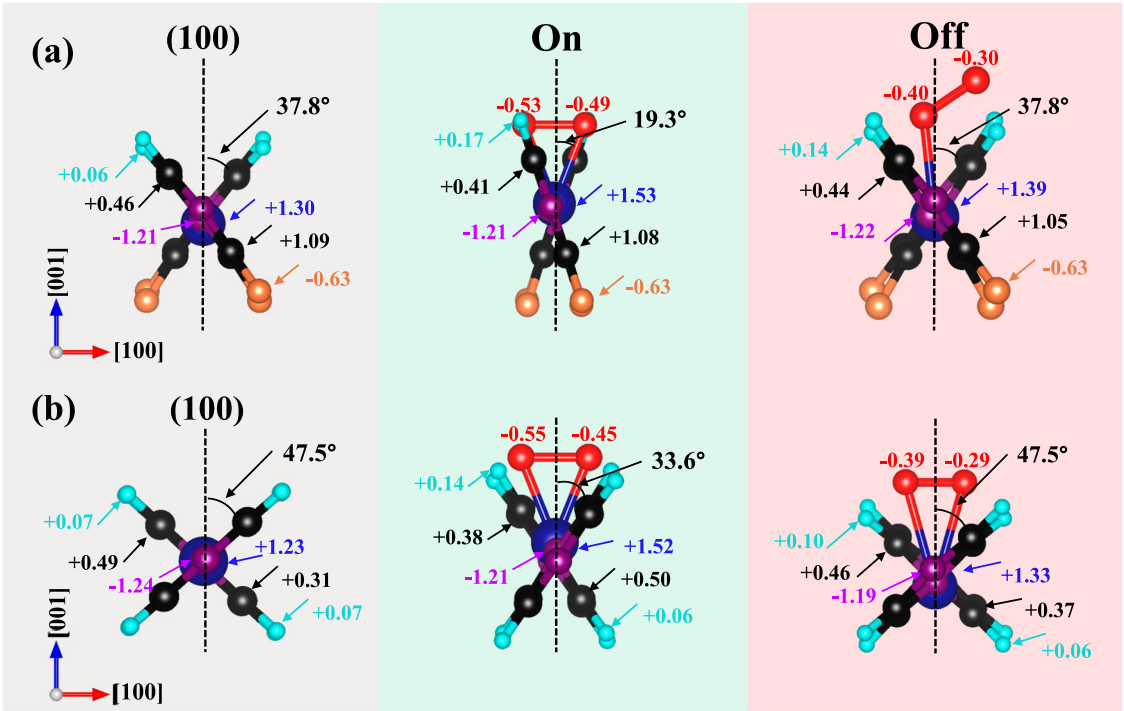

Fig. 6 | Comparison of charge transfer around active sites with On-Off ligand rotation of the two materials. Bader charges analysis for the cases of (**a**) Cr(h-fpyz)$_2$ and (**b**) Cr(pyz)$_2$ systems in the left panels shaded in gray and those with O_2 adsorption. In the central panels shaded in shallow green with O_2 adsorption, the structures are optimized without any constraints, i.e., ligand rotation is turned on. In the right panels shaded in pink, the angles of the organic ligands and the positions of Cr atoms are fixed to that in the pristine Cr(h-fpyz)$_2$ and Cr(pyz)$_2$, i.e., ligand rotation is turned off upon O_2 adsorption. Positive and negative values represent charge depletion and accommodation, respectively.

exhibits modest (considerable) upward shifts along the [010] (0.22 Å) and [100] (0.76 Å) direction.

However, quantitatively, the changes in relative angles of the organic ligands during the key steps of the CO oxidation on the multiferroic Cr(h-fpyz)$_2$ are more pronounced compared to those observed in the monoferroic Cr(pyz)$_2$ system. For instance, in the TS_1 state, the angle change reaches approximately 51.3% (from 37.8° to 18.4°) for Cr(h-fpyz)$_2$, whereas it is about 39.2% (from 47.5° to 28.9°) for Cr(pyz)$_2$. Simultaneously, the upward shift of the Cr reactive site is more significant in Cr(pyz)$_2$ (0.90 Å) than in Cr(h-fpyz)$_2$ (0.82 Å), which may correspond to the relatively higher E_{bar} of the monoferroic Cr(pyz)$_2$ (0.659 eV) compared to multiferroic Cr(h-fpyz)$_2$ (0.325 eV). This difference is attributed to the relatively large energy cost associated with the upward shift of the Cr atom compared to the rotation of the organic ligands (Supplementary Fig. 13).

The rotations of the organic ligands and the upward shift of the Cr reactive site effectively promote charge transfer from the substrate, specifically involving nearby *p*-block elements H and C, and *d*-block Cr atoms, to the O_2 molecule (Fig. 6). To investigate this phenomenon, we performed Bader charge analysis on the optimized structures of O_2 adsorption on both 2D multiferroic Cr(h-fpyz)$_2$ and monoferroic Cr(pyz)$_2$ systems, considering scenarios with and without allowing the rotations of the organic ligands and the accompanied upward shifts of the Cr atom. Specifically, when an O_2 molecule adsorbs freely on multiferroic Cr(h-fpyz)$_2$, the O_2 species acquires a charge of approximately 1.02 |e|, with the underlying Cr reactive site, the nearby C and H atoms donating about 0.23, −0.05, and 0.11 |e| per atom, respectively. However, for the case without rotation of the organic ligands and the accompanied upward shift of the Cr atom, the charge on the adsorbed O_2 molecule decreases to about 0.70 |e|, with the reactive Cr atom and the nearby H atoms at relatively greater distances donating about 0.09 |e| and 0.08 |e| per H atom, respectively (see Fig. 6a). A similar trend is also evident in the case of O_2 adsorption on the monoferroic Cr(pyz)$_2$. Specifically, for the case of with (without) free rotations of the ligands as shown in Fig. 6b, the adsorbed O_2 is charged by about 1.0 (0.68) |e|, with the underlying Cr reactive site, the nearby C and H atoms donating about 0.29 (0.10) |e|, −0.11 (−0.03) and 0.07 (0.03) |e| per atom, respectively. Moreover, the analysis of the local spin moment of the optimized O_2-Cr(pyz)$_2$ complex is also performed. Specifically, in the monoferroic Cr(pyz)$_2$, the magnetic moment of the adsorbed O_2 on Cr is reduced from 2.0 to −0.08 μ_B. Correspondingly, the magnetic moment of the Cr atom is reduced from 3.67 to 2.95 μ_B, with a reduction of 0.72 μ_B. The non-metal atoms, majorly the C and N in the vicinity of the reactive Cr atom, accommodate a magnetic moment of 0.77 μ_B, which is lower than the value of 0.83 μ_B in the case of O_2-Cr(h-fpyz)$_2$. Moreover, the effect of ligands rotation on the spin accommodations are further comparatively analyzed in the Supplementary Fig. 14. Collectively, the contrasting geometric structure changes between the multiferroic Cr(h-fpyz)$_2$ and monoferroic Cr(pyz)$_2$ systems upon O_2 adsorption result in quantitively distinct charge transfers and spin accommodations between the O_2 molecule and the substrate atoms. Importantly, such disparate charge transfers upon O_2 adsorptions result in distinct LEF surrounding the O_2 species, which are destined to significantly influence the oxidation of the polar molecule CO, as confirmed in the following section.

Crucial role of LEF surrounding the adsorbed O_2 in CO oxidation rate

The contrasting charge transfer and spin accommodations, due to the disparate rotations of the ligands within the two typical catalytic substrates, result in significant contrast LEF surrounding the O_2 species (Fig. 7a). Specifically, we present comparative electric field analyses for the optimized structures of O_2 adsorption on both catalytic complexes along the normal, indicated by the yellow solid arrow (Fig. 7a). The yellow dashed line marks the path through which the arrow runs, representing the position of the CO molecule in the transition state.

https://doi.org/10.1038/s41467-025-56863-1

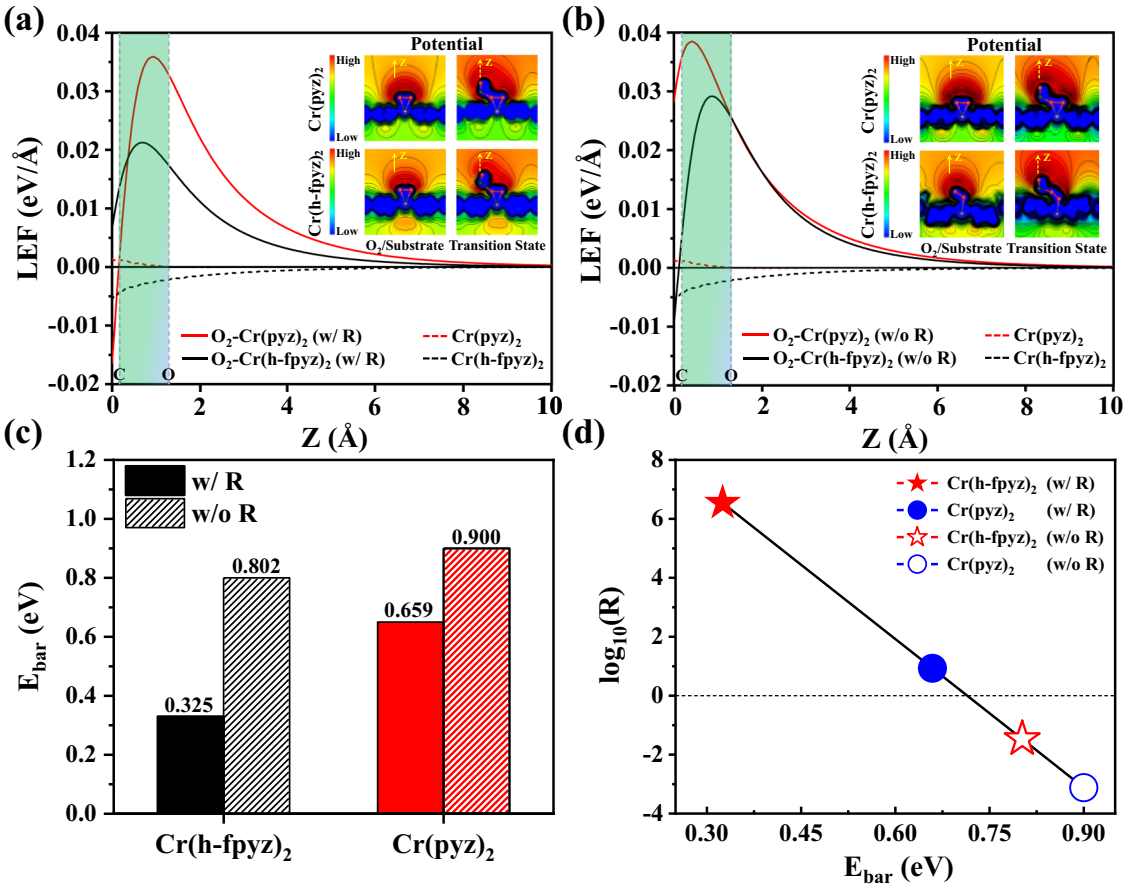

Fig. 7 | Effects of ligand rotations on local electric fields (LEF) and rate-limiting barriers (E_{bar}). **a** One-dimensional LEF profiles (solid lines) around the adsorbed O_2 along the normal directions of the substrates, as navigated by the yellow solid lines of the insets. The yellow dashed line marks the path through which the arrow runs, representing the position of the CO molecule in the transition states shown in Fig. 5a and Supplementary Fig. 15. The dashed lines correspond to the cases without O_2 adsorption, i.e., the pristine substrates. The green shaded part indicates the zone that covers the CO molecule. The insets illustrate the two-dimensional electrostatic potential contours right above the adsorbed O_2 and the CO-O_2 species of the TS state. **b** LEF obtained with the same approach as that in (**a**) with allowing the organic ligands rotations (w/ R), nevertheless without allowing the organic ligands rotations and upward shift of the Cr atoms, as simply termed w/o R. **c** Rate-limiting activation energy barriers (E_{bar}) for CO oxidation with (without) allowing the organic ligands rotations and upward shift of the Cr atoms (w/ R (w/o R)). **d** Logarithms of reaction rate of the CO oxidation on the multiferroic Cr(h-fpyz)$_2$ and monoferroic Cr(pyz)$_2$ for the cases of w/ R and w/o R.

Our DFT calculations demonstrate a significantly higher positive electric field for monoferroic Cr(pyz)$_2$ (indicated by the red solid line in Fig. 7a) compared to multiferroic Cr(h-fpyz)$_2$ (black solid line in Fig. 7a). Notably, in the transition state, the CO molecule is positioned nearly vertically above the O_2 molecule at similar heights for both Cr(pyz)$_2$ and Cr(h-fpyz)$_2$ cases. During CO oxidation, the CO molecule prefers a downward orientation towards the C atom when reacting with the activated O_2 molecule. This orientation results in stronger repulsive interactions between the polar CO molecule and the positive electric field surrounding the adsorbed O_2 molecule on monoferroic Cr(pyz)$_2$ compared to multiferroic Cr(h-fpyz)$_2$. Consequently, the significantly lower rate-limiting E_{bar} observed in the multiferroic Cr(h-fpyz)$_2$ underscores its enhanced catalytic efficiency compared to monoferroic Cr(pyz)$_2$. Note that, our DFT calculations can be further supported by a simple point-charge model analysis with and without considering the screening effects (Supplementary Fig. 16), where an asymmetric charge distribution between Cr and O_2 molecule can lead to an unexpected positive electric field (Supplementary Fig. 17).

Furthermore, for comparison, we have also calculated the rate-limiting E_{bar} of the CO oxidation on both multiferroic Cr(h-fpyz)$_2$ and monoferroic Cr(pyz)$_2$, without allowing the rotations of the organic ligands and upward shift of the Cr atoms (w/o R), *i.e.*, fixing them the same as that in the pristine substrate. When the organic ligands do not rotate, the CO molecule experiences stronger electrostatic repulsion (Fig. 7b). As a consequence, the barrier rises significantly from 0.325 (0.659) eV to 0.802 (0.900) eV in Cr(h-fpyz)$_2$ (Cr(pyz)$_2$) (Fig. 7c). Such an elevated E_{bar} results in a dramatically reduced reaction rate of 3.36×10^{-2} s^{-1} (7.60×10^{-4} s^{-1}). To more clearly demonstrate the relative importance of the flexibility of the organic ligand and the metal reactive site in the multiferroic Cr(h-fpyz)$_2$ and monoferroic Cr(pyz)$_2$ for CO oxidation, in Fig. 7d, we have further represented the reaction rates in the form of logarithms for the cases of both w/ R and w/o R. These findings further demonstrate that, the flexible rotation of the organic ligand and the metal reactive site can function as a tuning knob, lowing the rate-limiting E_{bar} for CO oxidation and enabling on-off switching the room-temperature catalysis in single-atom catalysts.

Discussion

Employing first-principles calculations based on density functional theory, we demonstrate that the 2D multiferroic structure of Cr(h-fpyz)$_2$ functions effectively as a room-temperature single-atom catalyst. This is evidenced by its highly enhanced catalytic activity, as highlighted by the following key findings:

(i) The calculated rate-limiting energy barrier for CO oxidation on the Cr single-atom reactive site within the 2D multiferroic catalytic platform is approximately 0.325 eV, resulting in a reaction rate of 3.47×10^{6} s^{-1} at room temperature and 1.34×10^{8} s^{-1} at 423 K, respectively, implying that the present

2D RT-MF Cr(h-fpyz)$_2$ is a promising high-performance catalytic candidate subject to "the 150 °C challenge" of US-DOE. This rate is six orders of magnitude higher than its monoferroic derivative, [Cr(pyz)$_2$]. Moreover, reversing the polar direction (rotating the organic ligands) of the 2D multiferroic Cr(h-fpyz)$_2$ structure reduces the reaction rate by eleven (eight) orders of the magnitude, enabling on-off switching of room-temperature catalysis of the 2D multiferroic system. Moreover, it seems that the present conclusion could also be generalized to some three-dimensional (3D) multiferroic catalytic platforms, such as the 3D Cr(h-fpyz)$_2$ counterpart, as detailed in Supplementary Fig. 18.

(ii) The underlying microscopic mechanism involves the activation of spin-triplet O_2 molecule, facilitated by more flexible rotations of the organic ligand around the Cr single-atom reactive site within the multiferroic Cr(h-fpyz)$_2$ complex compared to its monoferroic Cr(pyz)$_2$ derivative. This flexibility enhances the charge transfer and spin-accommodation processes, predominantly influenced by spin-polarized *p*-block substrate atoms and the confined *d*-block Cr single-atom reactive site.

(iii) Intriguingly, on the multiferroic Cr(h-fpyz)$_2$, O_2 adsorption induces a significantly lower local positive electric field normal to the surface compared to the Cr(pyz)$_2$, as supported by a simple point-charge model calculation. Consequently, the polar CO molecule experiences reduced repulsive electrostatic interactions and a considerably lower reaction energy barrier. Further simulations confirm that, without allowing the rotations of the organic ligands, the CO oxidation rate is dramatically reduced due to an increased rate-limiting energy barrier, by at least eight orders of magnitude.

(iv) The present findings are expected to offer new insights into establishing highly efficient single-atom catalyst platforms based on 2D multiferroics for a variety of other important chemical processes, such as NO oxidation, oxygen evolution reaction, oxygen reduction reaction, and photocatalysis on water splitting, wherein the charge, spin, and polarity degrees of freedom universally play significant roles.

Methods

Our calculations were carried out by spin-polarized first-principles calculations based on density functional theory (DFT)[64,65], as implemented in the Vienna ab initio simulation package (VASP)[66,67] with the version of VASP. 5. 4. 4, with the projector augmented wave (PAW)[68,69] method and the revised Perdew-Burke-Ernzerhof (RPBE)[70] for the exchange-correlation functional. DFT + U method[71,72] with U_{eff} = 4 eV is employed to treat the localization of 3 *d* orbitals of Cr atoms, as suggested by previous theoretical calculations[26]. The electronic wave functions were expanded in a plane wave basis with an energy cutoff of 550 eV, and the k-space integration was performed with a 2 × 2 × 1 Monkhorst-Pack k-point mesh in the Brillouin zone for the relatively large simulation cell. A vacuum space beyond 12 Å along the c-axis is incorporated to prevent interactions between neighboring slabs. To attain the optimized structures, all the atoms were allowed to relax until all the residual force components were less than 0.02 eV/Å. The kinetic properties of CO oxidation were investigated using the climbing-image nudged elastic band (CI-NEB) method[73,74], with the convergence criterion for electronic step within 10^{-5} eV and the total energy within 1 meV.

Data availability

The data supporting the findings of the study are included in the main text and supplementary information files.

References

1. Jones, J. et al. Thermally stable single-atom platinum-on-ceria catalysts via atom trapping. *Science* **353**, 150–154 (2016).
2. Aitbekova, A. et al. Templated encapsulation of platinum-based catalysts promotes high-temperature stability to 1,100 °C. *Nat. Mater.* **21**, 1290–1297 (2022).
3. Zammit, M., et al. *Future automotive aftertreatment solutions: The 150 °C challenge workshop report;* (US Department of Energy, 2013).
4. Yoon, B. et al. Charging effects on bonding and catalyzed oxidation of CO on Au_8 clusters on MgO. *Science* **307**, 403–407 (2005).
5. Zhong, W. H. et al. Electronic spin moment as a catalytic descriptor for Fe single-atom catalysts supported on C_2N. *J. Am. Chem. Soc.* **143**, 4405–4413 (2021).
6. Fu, Z. M., Yang, B. W. & Wu, R. Q. Understanding the activity of single-atom catalysis from frontier orbitals. *Phys. Rev. Lett.* **125**, 156001 (2020).
7. Le, C., Liang, Y. F., Evans, R. W., Li, X. M. & MacMillan, D. W. C. Selective sp^3 C-H alkylation via polarity-match-based cross-coupling. *Nature* **547**, 79–83 (2017).
8. Lv, Q. L., Zhu, Z., Ni, Y. X., Geng, J. R. & Li, F. J. Spin-state manipulation of two-dimensional metal–organic framework with enhanced metal–oxygen covalency for lithium-oxygen batteries. *Angew. Chem. Int. Ed.* **61**, e202114293 (2022).
9. Zhang, L. Y. et al. Synergetic charge transfer and spin selection in CO oxidation at neighboring magnetic single-atom catalyst sites. *Nano Lett.* **22**, 3744–3750 (2022).
10. Nair, A. N. et al. Spin-selective oxygen evolution reaction in chiral iron oxide nanoparticles: Synergistic impact of inherent magnetic moment and chirality. *Nano Lett.* **23**, 9042–9049 (2023).
11. Wigner, E. P. & Witmer, E. E. Über die struktur der zweiatomigen molekelspektren nach der quantenmechanik. *Z. Phys.* **51**, 859–886 (1928).
12. Moore, J. H. Investigation of the wigner spin rule in collisions of N^+ with He, Ne, Ar, N_2, and O_2. *Phys. Rev. A* **8**, 2359–2362 (1973).
13. Behler, J., Delley, B., Lorenz, S., Reuter, K. & Scheffler, M. Dissociation of O_2 at Al(111): The role of spin selection rules. *Phys. Rev. Lett.* **94**, 036104 (2005).
14. Carbogno, C., Behler, J., Gross, A. & Reuter, K. Fingerprints for spin-selection rules in the interaction dynamics of O_2 at Al(111). *Phys. Rev. Lett.* **101**, 096104 (2008).
15. Burgert, R. et al. Spin conservation accounts for aluminum cluster anion reactivity pattern with O_2. *Science* **319**, 438–442 (2008).
16. Aragonès, A. C. et al. Electrostatic catalysis of a diels–alder reaction. *Nature* **531**, 88–91 (2016).
17. Zhu, C. et al. High electric fields on water microdroplets catalyze spontaneous and fast reactions in halogen-bond complexes. *J. Am. Chem. Soc.* **145**, 21207–21212 (2023).
18. Ju, L. et al. Controllable CO_2 electrocatalytic reduction via ferroelectric switching on single atom anchored In_2Se_3 monolayer. *Nat. Commun.* **12**, 5128 (2021).
19. Liu, Y. et al. Bipolar charge collecting structure enables overall water splitting on ferroelectric photocatalysts. *Nat. Commun.* **13**, 4245 (2022).
20. Kakekhani, A., Ismail-Beigi, S. & Altman, E. I. Ferroelectrics: A pathway to switchable surface chemistry and catalysis. *Surf. Sci.* **650**, 302–316 (2016).
21. Wang, J. et al. Epitaxial $BiFeO_3$ multiferroic thin film heterostructures. *Science* **299**, 1719–1722 (2003).
22. Kimura, T. et al. Magnetic control of ferroelectric polarization. *Nature* **426**, 55–58 (2003).
23. Seixas, L., Rodin, A. S., Carvalho, A. & Neto, A. H. C. Multiferroic two-dimensional materials. *Phys. Rev. Lett.* **116**, 206803 (2016).
24. Eerenstein, W., Mathur, N. D. & Scott, J. F. Multiferroic and magnetoelectric materials. *Nature* **442**, 759–765 (2006).
25. Ramesh, R. & Spaldin, N. A. Multiferroics: Progress and prospects in thin films. *Nat. Mater.* **6**, 21–29 (2007).
26. Yang, Y. L. et al. Two-dimensional organic-inorganic room-temperature multiferroics. *J. Am. Chem. Soc.* **144**, 14907–14914 (2022).

27. Shi, P. P. et al. Two-dimensional organic–inorganic perovskite ferroelectric semiconductors with fluorinated aromatic spacers. *J. Am. Chem. Soc.* **141**, 18334–18340 (2019).
28. Sha, T. T. et al. Fluorinated 2D lead Iodide perovskite ferroelectrics. *Adv. Mater.* **31**, 1901843 (2019).
29. Tang, Y. Y. et al. Record enhancement of phase transition temperature realized by H/F substitution. *Adv. Mater.* **32**, 2003530 (2020).
30. Perlepe, P. et al. Metal-organic magnets with large coercivity and ordering temperatures up to 242 °C. *Science* **370**, 587–592 (2020).
31. Zhang, W. & Xiong, R. G. Ferroelectric metal-organic frameworks. *Chem. Rev.* **112**, 1163–1195 (2012).
32. Li, H. Y., Zhao, S. N., Zang, S. Q. & Li, J. Functional metal-organic frameworks as effective sensors of gases and volatile compounds. *Chem. Soc. Rev.* **49**, 6364–6401 (2020).
33. G-Saiz, P. et al. Metal-organic frameworks for dual photo-oxidation and capture of arsenic from water. *ChemSusChem* **17**, e202400592 (2024).
34. Qiao, B. T. et al. Single-atom catalysis of CO oxidation using Pt_1/FeO_x. *Nat. Chem.* **3**, 634–641 (2011).
35. Zhao, K. et al. Selective electroreduction of CO_2 to acetone by single copper atoms anchored on N-doped porous carbon. *Nat. Commun.* **11**, 2455 (2020).
36. Zhang, Z. L. et al. Thermally stable single atom Pt/m-Al_2O_3 for selective hydrogenation and CO oxidation. *Nat. Commun* **8**, 16100 (2017).
37. Muravev, V. et al. Interface dynamics of Pd-CeO_2 single-atom catalysts during CO oxidation. *Nat. Catal.* **4**, 469–478 (2021).
38. Li, S. W. et al. Impact of the coordination environment on atomically dispersed Pt catalysts for oxygen reduction reaction. *ACS Catal.* **10**, 907–913 (2020).
39. Liu, X., Jiao, Y., Zheng, Y., Jaroniec, M. & Qiao, S. Z. Building up a picture of the electrocatalytic nitrogen reduction activity of transition metal single-atom catalysts. *J. Am. Chem. Soc.* **141**, 9664–9672 (2019).
40. Sun, Y. M. et al. Modulating electronic structure of metal-organic frameworks by introducing atomically dispersed Ru for efficient hydrogen evolution. *Nat. Commun.* **12**, 1369 (2021).
41. Okamura, M. et al. A pentanuclear iron catalyst designed for water oxidation. *Nature* **530**, 465–468 (2016).
42. Wang, Y. G., Mei, D. H., Glezakou, V.-A., Li, J. & Rousseau, R. Dynamic formation of single-atom catalytic active sites on ceria-supported gold nanoparticles. *Nat. Commun.* **6**, 6511 (2015).
43. Jiang, B. J. et al. Dynamically confined single-atom catalytic sites within a porous heterobilayer for CO oxidation via electronic antenna effects. *Phys. Rev. B* **107**, 205421 (2023).
44. Li, W. et al. Interlayer charge transfer regulates single-atom catalytic activity on electride/graphene 2D heterojunctions. *J. Am. Chem. Soc.* **145**, 4774–4783 (2023).
45. Xu, Z. et al. Why does single-atom photocatalysis work better than conventional photocatalysis? A study on ultrafast excited carrier and structure dynamics. *Nano Lett.***23**, 4023–4031 (2023).
46. Liu, K. et al. Insights into the activity of single-atom Fe-N-C catalysts for oxygen reduction reaction. *Nat. Commun.* **13**, 2075 (2022).
47. Zhang, Y. et al. d-p hybridization-induced "Trapping–coupling–conversion" enables high-efficiency Nb single-atom catalysis for Li–S batteries. *J. Am. Chem. Soc.* **145**, 1728–1739 (2023).
48. Li, Y. et al. Local spin-state tuning of iron single-atom electrocatalyst by s-coordinated doping for kinetics-boosted ammonia synthesis. *Adv. Mater.* **34**, 2202240 (2022).
49. Wang, R. G. et al. Tuning Fe spin moment in Fe–N–C catalysts to climb the activity volcano via a local geometric distortion strategy. *Adv. Sci.* **9**, 2203917 (2022).
50. Yu, Y. H. et al. Fe on Sb(111): Potential two-dimensional ferromagnetic superstructures. *ACS Nano* **11**, 2143–2149 (2017).
51. Yan, R. et al. Origin and acceleration of insoluble Li_2S_2–Li_2S reduction catalysis in ferromagnetic atoms-based lithium-sulfur battery cathodes. *Angew. Chem. Int. Ed.* **62**, e202215414 (2023).
52. Kolpak, A. M., Grinberg, I. & Rappe, A. M. Polarization effects on the surface chemistry of $PbTiO_3$-supported Pt films. *Phys. Rev. Lett.* **98**, 166101 (2007).
53. Hwang, J. et al. Tuning perovskite oxides by strain: Electronic structure, properties, and functions in (electro)catalysis and ferroelectricity. *Mater. Today* **31**, 100–118 (2019).
54. Zhang, J. J. et al. Type-II multiferroic $Hf_2VC_2F_2$ mxene monolayer with high transition temperature. *J. Am. Chem. Soc.* **140**, 9768–9773 (2018).
55. Xu, M. L. et al. Electrical control of magnetic phase transition in a type-I multiferroic double-metal trihalide monolayer. *Phys. Rev. Lett.* **124**, 067602 (2020).
56. Wu, Y. L., Zhang, D. J., Zhang, Y.-N., Deng, L. J. & Peng, B. Nonreciprocal and Nonvolatile Electric-Field Switching of Magnetism in van der Waals Heterostructure Multiferroics. *Nano Lett.* **24**, 5929–5936 (2024).
57. Suo, H. et al. Covalent-bond-linked monolayer fullerene network as a spin sponge for spin-triplet O_2 activation and CO oxidation. *Phys. Rev. B* **110**, 125405 (2024).
58. Arrhenius, S. Ü. ber die reaktionsgeschwindigkeit bei der Inversion von rohrzucker durch säuren. *Z. Phys. Chem.* **4**, 226–248 (1889).
59. Ren, Y. et al. Unraveling the coordination structure-performance relationship in Pt_1/Fe_2O_3 single-atom catalyst. *Nat. Commun.* **10**, 4500 (2019).
60. Daelman, N., Capdevila-Cortada, M. & López, N. Dynamic charge and oxidation state of Pt/CeO_2 single-atom catalysts. *Nat. Mater.* **18**, 1215–1221 (2019).
61. Lu, Y. B. et al. Identification of the active complex for CO oxidation over single-atom Ir-on-$MgAl_2O_4$ catalysts. *Nat. Catal.* **2**, 149–156 (2019).
62. Wang, Y. et al. Electron penetration triggering interface activity of Pt-graphene for CO oxidation at room temperature. *Nat. Commun.* **12**, 5814 (2021).
63. Chen, W. Y. et al. Molecular-level insights into the electronic effects in platinum-catalyzed carbon monoxide oxidation. *Nat. Commun.* **12**, 6888 (2021).
64. Hohenberg, P. & Kohn, W. Inhomogeneous electron gas. *Phys. Rev.* **136**, B864–B871 (1964).
65. Kohn, W. & Sham, L. J. Self-consistent equations including exchange and correlation effects. *Phys. Rev.* **140**, A1133–A1138 (1965).
66. Kresse, G. & Furthmüller, J. Efficiency of ab-initio total energy calculations for metals and semiconductors using a plane-wave basis set. *Comput. Mater. Sci.* **6**, 15–50 (1996).
67. Kresse, G. & Furthmüller, J. Efficient iterative schemes for ab initio total-energy calculations using a plane-wave basis set. *Phys. Rev. B* **54**, 11169–11186 (1996).
68. Blöchl, P. E. Projector augmented-wave method. *Phys. Rev. B* **50**, 17953–17979 (1994).
69. Kresse, G. & Joubert, D. From ultrasoft pseudopotentials to the projector augmented-wave method. *Phys. Rev. B* **59**, 1758–1775 (1999).
70. Hammer, B., Hansen, L. B. & Nørskov, J. K. Improved adsorption energetics within density-functional theory using revised perdew-burke-ernzerhof functionals. *Phys. Rev. B* **59**, 7413–7421 (1999).
71. Anisimov, V. I., Zaanen, J. & Andersen, O. K. Band theory and Mott insulators: Hubbard U instead of Stoner I. *Phys. Rev. B* **44**, 943–954 (1991).

72. Anisimov, V. I., Solovyev, I. V., Korotin, M. A., Czyżyk, M. T. & Sawatzky, G. A. Density-functional theory and NiO photoemission spectra. *Phys. Rev. B* **48**, 16929–16934 (1993).
73. Henkelman, G., Uberuaga, B. P. & Jónsson, H. A climbing image nudged elastic band method for finding saddle points and minimum energy paths. *J. Chem. Phys.* **113**, 9901–9904 (2000).
74. Henkelman, G. & Jónsson, H. Improved tangent estimate in the nudged elastic band method for finding minimum energy paths and saddle points. *J. Chem. Phys.* **113**, 9978–9985 (2000).

Acknowledgements

F.X.Z. and P.S.W. contributed equally to this work. We thank Prof. Zhenyu Zhang for the helpful discussion. This work was supported by the NSF of China (Grants No. U23A2072 (S.F.L.), 12074345 (S.F.L.), 12174349 (X.Y.R.), 12204431 (J. L.S.). The calculations were performed at the National Supercomputing Center in Zhengzhou, Henan.

Author contributions

S.F.L. and X.Y.R. conceived the idea and designed the work; F.X.Z. performed the calculations; P.S.W. conducted the mechanism analysis and model calculations; S.F.L., X.Y.R., F.X.Z., and P.S.W. wrote the manuscript; Y.D.Z., J.L.S., and R.P. participated in the discussion on the data and mechanism analysis. All authors contributed to the preparation of the manuscript.

Competing interests

The authors declare no competing interests.

Additional information

Supplementary information The online version contains supplementary material available at https://doi.org/10.1038/s41467-025-56863-1.

Correspondence and requests for materials should be addressed to Xiaoyan Ren or Shunfang Li.

Peer review information *Nature Communications* thanks Jun Jiang, Han Seul Kim, and the other anonymous reviewer(s) for their contribution to the peer review of this work. A peer review file is available.